Parity doublet bands in ^{223}Th within reflection-asymmetric triaxial particle rotor model

Y. Y. Wang *

Mathematics and Physics Department, North China Electric Power University, Beijing 102206, China
and State Key Laboratory of Nuclear Physics and Technology, School of Physics, Peking University, Beijing 100871, China

(Received 31 May 2021; accepted 12 July 2021; published 27 July 2021)

The recently updated parity doublet structures in ^{223}Th are investigated by using the reflection-asymmetric triaxial particle rotor model. The calculated results well reproduce the available data of the energy spectra and the $B(E1)/B(E2)$ ratios for both medium spin region and the newly established higher spin region, as well as the average value of $B(M1)/B(E2)$ for spins $9/2\hbar$ and $11/2\hbar$ in the positive-parity band. The main components of the intrinsic wave functions are analyzed to investigate the intrinsic wave functions and their evolutions with spin. The parity doublet bands are mainly based on a single neutron configuration, in which the largest component of the intrinsic wave function is $\nu(g_{9/2}, j_{15/2})[\Omega = 5/2]$ and the second largest one is $\nu(g_{9/2}, j_{15/2})[\Omega = 3/2]$. The amplitude of the largest component decreases whereas the second largest one increases with increasing spin, and the signature splitting behavior for the parity doublet bands could be understood by the variation of these main components with spin.

DOI: 10.1103/PhysRevC.104.014318

I. INTRODUCTION

The atomic nucleus is a microscopic quantum many-body system, and its shape provides an intuitive understanding of nuclear spatial density distributions [1,2]. The existence of stable quadrupole-deformed nuclear shapes with axial symmetry in the intrinsic frame has been known for a long time. All members of the observed rotational bands have the same parity since such shape is symmetric under the space reflection operation. However, with the first observation of the low-lying negative-parity states near the ground state in even-even Ra isotopes [3,4], the possibility arose that some nuclei might have an asymmetric shape under space reflection, such as a pear shape.

Nowadays, the structure of pear-shaped nuclei has been at the frontiers of both nuclear and particle physics, since it provides a unique probe to test the charge-parity (CP) violation beyond the standard model [5]. The pear shapes of a nucleus arise from the strong octupole correlations of the nucleons near the Fermi surface occupying states of opposite parity with orbital and total angular momentum differing by $3\hbar$, i.e., $\Delta l = \Delta j = 3\hbar$. Empirically, this condition occurs predominantly in nuclei with proton (neutron) numbers 34 ($g_{9/2} \leftrightarrow p_{3/2}$), 56 ($h_{11/2} \leftrightarrow d_{5/2}$), 88 ($i_{13/2} \leftrightarrow f_{7/2}$), and 134 ($j_{15/2} \leftrightarrow g_{9/2}$), characterized by the occurrence of, e.g., the interleaved positive- and negative-parity bands in even-even nuclei, the parity doublet bands in odd-mass nuclei, and the enhanced electric-dipole ($E1$) transitions [6–8].

So far, the octupole correlations and the pear-shaped nuclei have been studied extensively in the $A \approx 150$ mass region with $Z \approx 56$ and $N \approx 88$, and in the $A \approx 220$ mass region with $Z \approx 88$ and $N \approx 134$, see the reviews [6–8]. Evidence for octupole correlations in the $A \approx 80$ mass region has also been observed [9,10], which opens a new territory of investigation of octupole correlations.

Octupole-deformed nuclei with an odd nucleon have attracted special interest since they have enhanced nuclear Schiff moments [6,11–15]. Over the past decades considerable efforts have been devoted to study the excited states in odd-mass nuclei characterized by static and dynamic octupole deformation, see, e.g., Refs. [16–32]. Theoretically, various approaches have been developed to study the observed experimental features in odd-mass nuclei, such as the particle rotor model [33–35], the microscopic core-quasiparticle coupling model [36], the coherent quadrupole-octupole model [37,38], the cluster model [39], the reflection asymmetric shell model [40–42], and the interacting boson-fermion model [43].

Focusing on the thorium isotopes, the nucleus ^{223}Th has often been cited as one of the best cases of parity doublet bands, considering the nearly degenerate bands with opposite parities, the enhanced $E1$ transitions, and the nearly identical g factors for the opposite parity bands [44,45]. The parity doublet structures observed in ^{223}Th were interpreted in terms of an octupole-deformed core coupled to an unpaired nucleon in Ref. [44]. In Ref. [16], $14E2$ and $11E1$ transitions have been added to the parity doublet structures with ^{223}Th the positive and negative parity, which have been extended from $31/2^+$ to $49/2^+$ and from $31/2^-$ to $47/2^-$, respectively. The splitting of the parity doublet bands shows an oscillation behavior, and a backbending and an upbending appear at spin-parity $49/2^+$ and $47/2^-$, respectively. A further study is interesting to investigate the updated spectroscopy information in ^{223}Th, to explore the parity doublet structures in the medium- and high-spin regions.

*yywang1021@pku.edu.cn

In this work, the newly developed reflection-asymmetric triaxial particle rotor model (RAT-PRM) [46] is applied to describe the observed parity doublet structures in ^{223}Th. This model has been successfully applied to investigate the multiple chiral doublet bands with octupole correlations in ^{73}Br [46], ^{131}Ba [47], and ^{124}Cs [48], and the novel structure for an ideal Chirality-Parity (ChP) violation system [49]. It also provides a useful tool for describing the octupole correlations in odd-mass pear-shaped nuclei and has been successfully applied to investigate the parity doublet bands observed in ^{143}Ba [50].

This paper is organized as follows: The model is briefly introduced in Sec. II and the numerical details are presented in Sec. III. The calculated results for the positive- and negative-parity bands, such as energy spectra and the electromagnetic transitions, are discussed in Sec. IV. A summary is given in Sec. V.

II. THEORETICAL FRAMEWORK

The detailed RAT-PRM formalism has been outlined in Ref. [46]. The total Hamiltonian is

$$\hat{H} = \hat{H}^{p(n)}_{\text{intr.}} + \hat{H}_{\text{core}}, \tag{1}$$

where $\hat{H}^{p(n)}_{\text{intr.}}$ is the intrinsic Hamiltonian for valence protons (neutrons) in a reflection-asymmetric triaxially deformed potential, and $\hat{H}_{\text{core}}$ is the Hamiltonian of a reflection-asymmetric triaxial rotor.

The core Hamiltonian $\hat{H}_{\text{core}}$ is generalized straightforwardly from the reflection-asymmetric axial rotor in Ref. [33],

$$\hat{H}_{\text{core}} = \sum_{k=1}^{3} \frac{\hat{R}_k^2}{2\mathcal{J}_k} + \frac{1}{2}E(0^-)(1-\hat{P}_c), \tag{2}$$

with $\hat{R}_k = \hat{I}_k - \hat{j}_{pk} - \hat{j}_{nk}$. Here, $\hat{R}_k$, $\hat{I}_k$, $\hat{j}_{pk}$, and $\hat{j}_{nk}$ are the angular-momentum operators for the core, the nucleus, the valence protons, and the valence neutrons, respectively. For the moments of inertia (MoIs), the irrotational flow type $\mathcal{J}_k = \mathcal{J}_0 \sin^2(\gamma - 2k\pi/3)$ is adopted. In the last term, the core parity splitting parameter $E(0^-)$ is treated as a free parameter to describe the excitation energy of the virtual 0^- state [33], and the core parity operator $\hat{P}_c$ is the product of the single-particle parity operator $\hat{\pi}$ and the total parity operator $\hat{P}$.

The intrinsic Hamiltonian $\hat{H}^{p(n)}_{\text{intr.}}$ for valence nucleons is [51–53]

$$\hat{H}^{p(n)}_{\text{intr.}} = \sum_{\nu>0} \left(\varepsilon^{p(n)}_{\nu} - \lambda\right)(a^{\dagger}_{\nu}a_{\nu} + a^{\dagger}_{\bar{\nu}}a_{\bar{\nu}}) - \frac{\Delta}{2}\sum_{\nu>0}(a^{\dagger}_{\nu}a^{\dagger}_{\bar{\nu}} + a_{\bar{\nu}}a_{\nu}), \tag{3}$$

where λ denotes the Fermi energy, Δ is the pairing gap parameter, and $|\bar{\nu}\rangle$ is the time-reversal state of $|\nu\rangle$. The single-particle energy $\varepsilon^{p(n)}_{\nu}$ is obtained by diagonalizing a single-particle Hamiltonian $\hat{H}^{p(n)}_{\text{s.p.}}$ that has the form of a Nilsson Hamiltonian [54],

$$\hat{H}^{p(n)}_{\text{s.p.}} = -\tfrac{1}{2}\hbar\omega_0\nabla^2 + V(r;\theta,\varphi) + C\boldsymbol{l}\cdot\boldsymbol{s} + D[\boldsymbol{l}^2 - \langle\boldsymbol{l}^2\rangle_N], \tag{4}$$

with the four terms being kinetic energy, the reflection-asymmetric triaxially deformed potential [46], the spin-orbit term, and the shifting term [2], respectively. The parameters C and D are related to the standard Nilsson parameters κ and μ with $C = -2\kappa$ and $D = -\kappa\mu$, respectively.

The total Hamiltonian $\hat{H}$ is diagonalized numerically in the symmetrized strong-coupled basis with good parity and angular momentum, which gives rise to the eigenvalues and eigen wave functions and which are used to calculate the reduced electromagnetic transition probabilities [46].

III. NUMERICAL DETAILS

In the present RAT-PRM calculations, the quadrupole and octupole deformation parameters are taken from Ref. [35], in which $\beta_2 = 0.12$, $\gamma = 0^\circ$, and $\beta_3 = 0.10$ were adopted for the parity doublet bands in ^{223}Th. With these deformation parameters, the reflection-asymmetric Nilsson Hamiltonian (4) with the parameters κ, μ in Ref. [55] is solved in the harmonic-oscillator basis [56]. The Fermi energy for neutrons in Eq. (3) is chosen as $\lambda_n = 49.64$ MeV, corresponding to the parity-mixed orbital $\nu(g_{9/2}, j_{15/2})[\Omega = 5/2]$. The single-particle space available to the odd nucleon is truncated to 13 levels, with six above and six below the Fermi level. Increasing the size of the single-particle space does not influence the band structure in the present calculations. The pairing gap is calculated by the empirical formula $\Delta = 12/\sqrt{A}$ MeV.

For the core part, it turns out that a spin-dependent MoI, i.e., $\mathcal{J}(I) = (\mathcal{J}_0 + bI)\ \hbar^2/\text{MeV}$ with $\mathcal{J}_0 = 45$ and $b = 1$, is necessary to reproduce the experimental energy spectra. This spin-dependent MoI can be attributed to the increasing behavior versus spin for the effective MoI extracted from the experimental data of the parity doublets in ^{223}Th [16,44]. The core parity splitting parameter $E(0^-) = 0.207$ MeV is obtained by taking the average experimental 1^- excitation energy in the two neighboring even-even nuclei [35]. It is well known that an *ad hoc* attenuation of the Coriolis couplings is generally needed in the PRM description [57]. In the present RAT-PRM calculation, the Coriolis attenuation factor is $\xi = 0.45$ for the positive-parity band and $\xi = 0.63$ for the negative-parity band. A smaller ξ for the positive-parity band is consistent with its smaller signature splitting than that for negative-parity band.

For the calculations of the electric-multipole transitions, the intrinsic electric-dipole moment $Q_{10} = 0.32\ e\,\text{fm}$ is adopted, which was determined empirically in Ref. [35], while the intrinsic quadrupole moment $Q_0 = (3/\sqrt{5\pi})R_0^2 Z\beta_2$ is calculated with $R_0 = 1.2A^{1/3}$ fm. For the calculation of the magnetic-dipole transitions, $g_n - g_R = -0.405$ is adopted, which is the average of the empirical values for the $7/2^+ \to 5/2^+$ and $9/2^+ \to 7/2^+$ transitions determined from the $M1/E2$ mixing ratios in Ref. [44].

IV. RESULTS AND DISCUSSION

The calculated excitation energies and the energy staggering parameters $S(I) = [E(I) - E(I-1)]/2I$ for the positive-parity band A and negative-parity band B in ^{223}Th by the

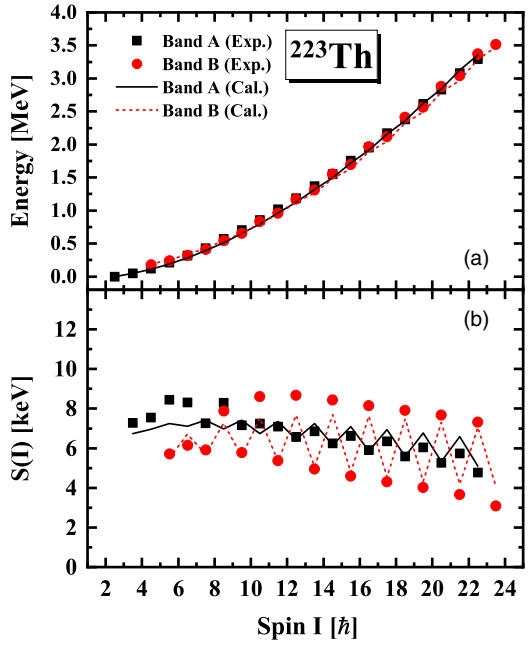

FIG. 1. (a) The calculated energies $E(I)$ and (b) the energy staggering parameters $S(I) = [E(I) - E(I-1)]/2I$ for the positive-parity band A and negative-parity band B in ^{223}Th by RAT-PRM (lines) in comparison with the experimental data [16] (symbols).

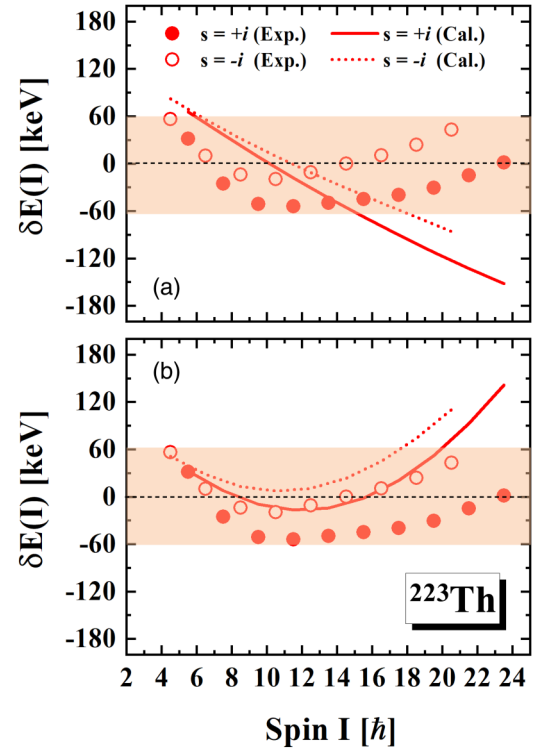

FIG. 2. The calculated parity splitting $\delta E(I)$ between the negative-parity state and the (interpolated) positive-parity state with simplex $s = +i$ and $-i$ in ^{223}Th by RAT-PRM (lines) in comparison with the available data [16] (symbols). Calculation results are shown in panel (a) with the same MoI for positive- and negative-parity bands ($\mathcal{J}_0 = 45$ and $b = 1.00$), and (b) with different MoIs for the positive-parity band ($\mathcal{J}_0 = 32$ and $b = 1.55$) and the negative-parity band ($\mathcal{J}_0 = 35$ and $b = 1.20$), respectively.

RAT-PRM are shown in Fig. 1 and compared with the available data [16].

As shown in Fig. 1(a), the calculated excitation energies well reproduce the data for both bands A and B. For the observed spin range of $9/2\hbar \leqslant I \leqslant 45/2\hbar$, the calculated average energy difference for the parity doublet bands is 56 keV, which is close to the experimental value of 37 keV. This small energy difference between parity doublets indicates the strong octupole correlations in this nucleus.

Figure 1(b) depicts the calculated $S(I)$ values in comparison with the experimental data. It can be seen that the negative-parity band B exhibits a pronounced signature splitting in contrast to the considerably smaller splitting observed for the positive-parity band A. For the positive-parity band A, the calculated $S(I)$ values reproduce the experimental data both in the staggering amplitude and phase within $I \geqslant 21/2\hbar$ spin region. For the negative-parity band, the staggering behavior of the $S(I)$ values is well reproduced by the present calculations.

To discuss the parity splitting, the energy difference $\delta E(I)$ between negative-parity states and the (interpolated) positive-parity states for a given spin has been extensively used [58],

$$\delta E(I) = E(I)^- - \frac{(I+1)E(I-1)^+ + IE(I+1)^+}{2I+1}. \quad (5)$$

These energy differences are plotted in Fig. 2 for the observed bands in ^{223}Th with simplex $s = +i$ and $-i$ by RAT-PRM and are compared with the available data [16].

It can be clearly seen from Fig. 2(a) that the experimental parity splitting $\delta E(I)$ shows a parabola trend with increasing spin, while the calculated values decrease linearly with spin. The experimental sign inversion of the parity splitting $\delta E(I)$ in the high-spin region is not reproduced by the calculation. Considering that, in this mass region, the negative-parity bands have a larger effective MoI in the lower-spin region than the positive-parity bands, which is related to a larger quadrupole deformation [59], the RAT-PRM calculations with different MoIs for the positive-parity band ($\mathcal{J}_0 = 32$ and $b = 1.55$) and the negative-parity band ($\mathcal{J}_0 = 35$ and $b = 1.20$) are performed. The other parameters in the calculation are kept unchanged. As shown in Fig. 2(b), the sign inversion and the parabolic trend of $\delta E(I)$ is now reproduced.

It should be mentioned that the sign inversion of the parity splitting has been extensively discussed in the literature [16,60,61]. In Ref. [60], Frauendorf proposed the concept of the condensation of the rotational-aligned octupole phonons and suggested that discrete phonon energy and parity conservation generate the sign inversion of parity splitting. The continued sign inversion of parity splitting was expected to be observed in the high-spin region in this interpretation [60]. Another interpretation was proposed by Jolos *et al.* in Ref. [61], in which the complicated behavior of the parity splitting was interpreted as the result of two simultaneous effects: (1) penetration of the barrier separating two minima with opposite signs of the octupole deformation and (2)

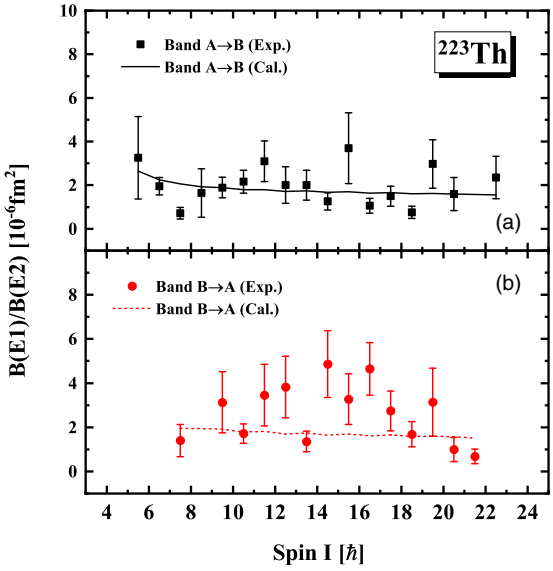

FIG. 3. The calculated $B(E1)/B(E2)$ ratios between the interband $E1$ transitions and the intraband $E2$ transitions in comparison with the available experimental data [16] for (a) band A → B and (b) band B → A.

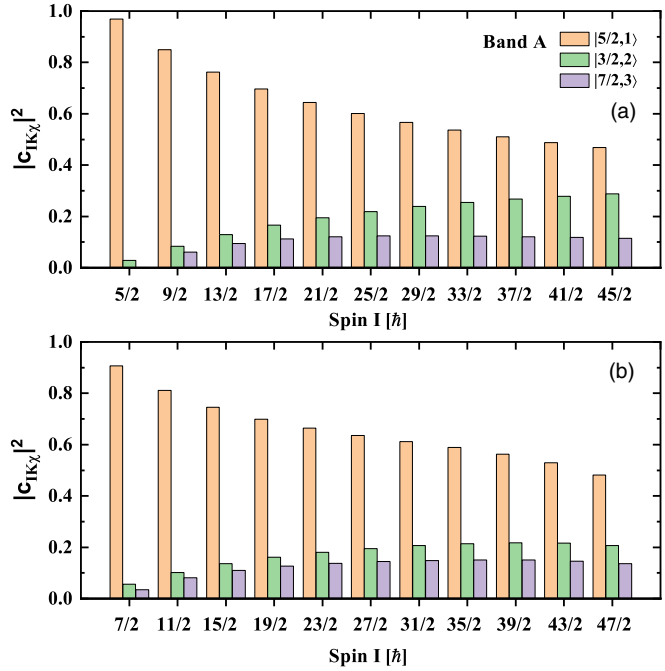

FIG. 4. The main components of the intrinsic wave functions expanded in the strong-coupled basis $|IMK\rangle\chi^{\nu}$ (denoted as $|K, \nu\rangle$ for short) for the positive-parity band A within spin region $\frac{5}{2}\hbar \leqslant I \leqslant \frac{47}{2}\hbar$. $|IMK\rangle$ is the Wigner function with I, M, and K being the quantum numbers of the total angular momentum and its projections along the third axis in the laboratory frame and intrinsic frame, respectively. The χ^{ν} represent the intrinsic wave functions of the neutron single-particle level $|\nu\rangle$ that obtained by diagonalizing the reflection-asymmetric Nilsson Hamiltonian.

alignment of the angular momentum of the intrinsic excitations. In the present work, although the sign inversion and the parabola trend of the parity splitting can be reproduced by using a different spin-dependent MoIs for the positive- and negative-parity bands, as shown in Fig. 2(b), the quantitative agreement is not satisfactory, which deserves further investigations in the future.

In addition to the degeneracy in the energy spectra, the observation of enhanced $E1$ transitions connecting the parity doublet bands also serves as important experimental evidence for octupole correlations in atomic nuclei. From the measured transition energies E_γ and branching ratios $I_\gamma(E1)/I_\gamma(E2)$ in ^{223}Th [16], one can extract the ratios $B(E1)/B(E2)$,

$$B(E1)/B(E2) = 0.771 \frac{E_\gamma^5(E2) I_\gamma(E1)}{E_\gamma^3(E1) I_\gamma(E2)} \ (10^{-6}\ \mathrm{fm}^{-2}). \quad (6)$$

Figures 3(a) and 3(b) show the calculated $B(E1)/B(E2)$ ratios between the interband $E1$ transitions starting from the positive- and the negative-parity states and the intraband $E2$ transitions in comparison with the available experimental data [16]. It can be seen that the experimental $B(E1)/B(E2)$ ratios with $E1$ transitions starting from the positive-parity and the negative-parity states are similar in general and can be well reproduced by the calculated results.

Furthermore, the two bands of opposite simplex observed in ^{223}Th are interconnected at low spins by strong magnetic-dipole transitions $M1$ [44]. These $M1$ transitions are sensitive to the single-particle components of the intrinsic wave functions. The experimental $B(M1)/B(E2)$ ratios are available for spins $9/2$ and $11/2$ in the positive-parity band A, and the average value for these two spins, $7.12(252) \times 10^{-6}\ \mu_N^2/(e^2\,\mathrm{fm}^4)$, was given in Ref. [24]. The present calculated average value for these two spins is $8.04 \times 10^{-6}\ \mu_N^2/(e^2\,\mathrm{fm}^4)$, which well reproduces the experimental data and indicates the proper intrinsic wave functions in the present calculations.

To further investigate the intrinsic wave functions and their evolution with spin, Figs. 4 and 5 show the main components of the intrinsic wave functions expanded in the strong-coupled basis $|IMK\rangle\chi^{\nu}$ for the positive parity band A and negative-parity band B, respectively. Here, $|IMK\rangle$ is the Wigner function with I, M, and K denoting the quantum numbers of the total angular momentum and its projections along the third axis in the laboratory frame and intrinsic frame, and χ^{ν} represents the intrinsic wave function of the neutron single-particle level $|\nu\rangle$. It can be seen from Figs. 4 and 5 that the main components of the intrinsic wave functions for the parity doublet bands are similar, and the top three components are $|5/2, 1\rangle$, $|3/2, 2\rangle$, and $|7/2, 3\rangle$, respectively. In the present calculations with $\beta_2 = 0.12$, $\gamma = 0^\circ$, and $\beta_3 = 0.10$, the main spherical harmonic-oscillator components $l_{j\Omega}$ for the neutron single-particle levels $|\nu\rangle$ with $\nu = 1, 2, 3$, are shown in Fig. 6. For each neutron single-particle level $|\nu\rangle$, since $\gamma = 0^\circ$ and $\beta_3 \neq 0$, Ω is a good quantum number and orbitals with opposite parity, e.g., $g_{9/2}$ and $j_{15/2}$, can mix with each other. The dominant components for levels $|1\rangle$, $|2\rangle$, and $|3\rangle$ are the same $g_{9/2}$ orbital but with different Ω components, $\Omega = 5/2$, $3/2$, and $7/2$, respectively.

As shown in Figs. 4 and 5, the top three components of the intrinsic wave functions for the parity doublet bands change

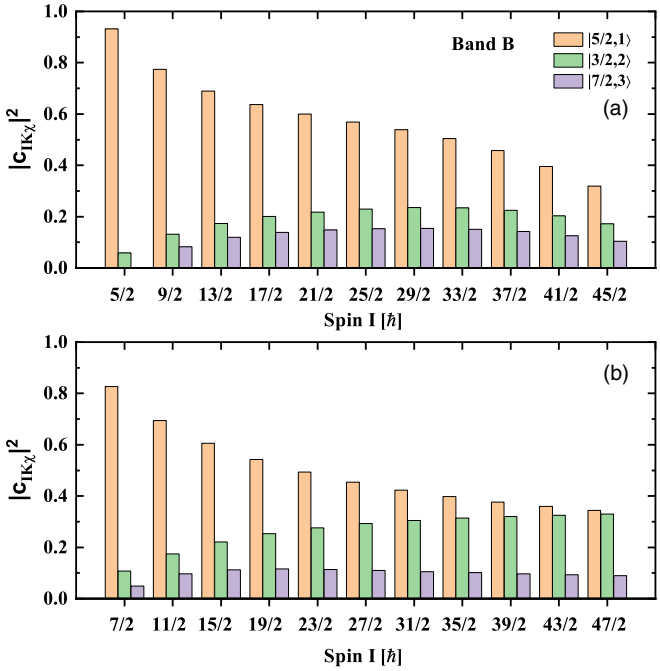

FIG. 5. Same as Fig. 4, but for the negative-parity band B.

with the increase of spin. It will be helpful to understand the different behaviors of the signature splitting for the parity doublet bands shown in Fig. 1(b) by analyzing the variation of these main components with spin.

For the positive-parity band A, as shown in Fig. 4, the largest component $|5/2, 1\rangle$ decreases with spin, while the second largest component $|3/2, 2\rangle$ increases with spin. To be more precise, for states with signature $+i$ $(5/2, 9/2, \dots)$ shown in Fig. 4(a), the amplitude of the largest component $|5/2, 1\rangle$ decreases from 0.969 (5/2) to 0.460 (45/2), whereas the second largest $|3/2, 2\rangle$ increases from 0.029 (5/2) to 0.290 (45/2). For the states with signature $-i$ $(7/2, 11/2, \dots)$ shown in Fig. 4(b), the amplitude of the largest component $|5/2, 1\rangle$ decreases from 0.906 (7/2) to 0.456 (47/2), whereas the second largest $|3/2, 2\rangle$ increases from 0.057 (7/2) to 0.199 (47/2). It is found that the decrease of $|5/2, 1\rangle$ and the increase of $|3/2, 2\rangle$ for the states with signature $+i$ are faster than those with signature $-i$. Considering the fact that the Coriolis effect for the single-particle level $|2\rangle$ with low-Ω ($\Omega = 3/2$) is stronger than in the level $|1\rangle$ with $\Omega = 5/2$ in the present axial case, the Coriolis effect for the states with signature $+i$ in band A is larger than those with signature $-i$. This leads to energies of the states with signature $+i$ which are favored over those with signature $-i$ and could explain the signature splitting shown in Fig. 1(b), in which the states with signature $+i$ are lower than those with signature $-i$.

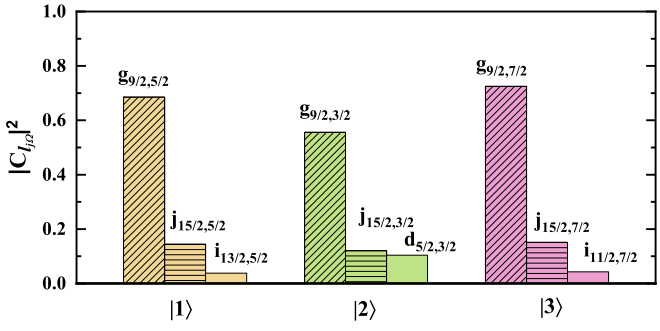

FIG. 6. The main components $l_{j\Omega}$ of the neutron single-particle levels $|\nu\rangle$ with $\nu = 1$, 2, and 3.

For the negative-parity band B as shown in Fig. 5, it is the same as band A, the largest component $|5/2, 1\rangle$ decreases with spin, whereas the second largest $|3/2, 2\rangle$ increases with spin. However, the decrease of $|5/2, 1\rangle$ and the increase of $|3/2, 2\rangle$ for the states with signature $+i$ are slower than those with signature $-i$. For the states with signature $+i$ the amplitude of the largest component $|5/2, 1\rangle$ decreases from 0.928 (5/2) to 0.250 (45/2), whereas the second largest $|3/2, 2\rangle$ increases from 0.062 (5/2) to 0.139 (45/2). Meanwhile, for the states with signature $-i$ the amplitude of the largest component $|5/2, 1\rangle$ decreases from 0.817 (7/2) to 0.331 (47/2), whereas the second largest $|3/2, 2\rangle$ increases from 0.113 (7/2) to 0.331 (47/2). Consequently, the Coriolis effect for the states with signature $+i$ in band B is smaller than those with signature $-i$, which leads to energies of the states with signature $+i$ which are unfavored than those with signature $-i$. This is contrary to the situation that occurred in the positive band A and can account for the opposite staggering phase for the positive- and negative-parity bands shown in Fig. 1(b).

V. SUMMARY

In summary, reflection-asymmetric triaxial particle rotor model calculations have been performed to investigate the recently updated parity doublet structures in ^{223}Th. The energy spectra, the energy staggering parameters, and the $B(E1)/B(E2)$ ratios for both medium spin and the newly established higher spin region, as well as the average value of $B(M1)/B(E2)$ for spins $9/2\hbar$ and $11/2\hbar$ in the positive-parity band are well reproduced by the present RAT-PRM calculations.

To further investigate the intrinsic wave functions and their evolutions with spin, the main components of the intrinsic wave functions are analyzed. It is found that the parity doublet bands are mainly based on a single neutron configuration that its largest component of the intrinsic wave function is $\nu(g_{9/2}, j_{15/2})[\Omega = 5/2]$, and the second largest one is $\nu(g_{9/2}, j_{15/2})[\Omega = 3/2]$. With the increase of spin, the amplitude of the largest component decreases whereas the second-largest one increases, and the signature splitting behavior for the parity doublet bands could be understood by the variation of these main components with spin. For the parity splitting, although its sign inversion and parabola trend can be reproduced by using a different spin-dependent MoIs for the positive- and negative-parity bands, the quantitative agreement is not satisfactory, which deserves further investigations in the future.

ACKNOWLEDGMENTS

Fruitful discussions with Professor Shuangquan Zhang are highly acknowledged. This work was partly supported by the China Postdoctoral Science Foundation (Grant No. 2020M670014), the National Natural Science Foundation of China (Grants No. 11875075, No. 11935003, and No. 12070131001), and the State Key Laboratory of Nuclear Physics and Technology, Peking University (Grant No. NPT2020ZZ01).

[1] A. Bohr and B. R. Mottelson, *Nuclear Structure* (Benjamin, New York, 1975), Vol. II.

[2] P. Ring and P. Schuck, *The Nuclear Many-Body Problem* (Springer Science & Business Media, Berlin, 2004).

[3] F. S. Stephens, F. Asaro, and I. Perlman, Phys. Rev. **96**, 1568 (1954).

[4] F. S. Stephens, F. Asaro, and I. Perlman, Phys. Rev. **100**, 1543 (1955).

[5] L. P. Gaffney, P. A. Butler, M. Scheck, A. B. Hayes, F. Wenander, M. Albers, B. Bastin, C. Bauer, A. Blazhev, S. Bönig, N. Bree, J. Cederkall, J. Chupp, D. Cline, T. E. Cocolios, T. Davinson, H. De Witte, J. Diriken, T. Grahn, A. Herzan *et al.*, Nature (London) **497**, 199 (2013).

[6] P. A. Butler and W. Nazarewicz, Rev. Mod. Phys. **68**, 349 (1996).

[7] P. A. Butler, J. Phys. G **43**, 073002 (2016).

[8] P. A. Butler, Proc. R. Soc. A **476**, 20200202 (2020).

[9] C. Liu, S. Y. Wang, R. A. Bark, S. Q. Zhang, J. Meng, B. Qi, P. Jones, S. M. Wyngaardt, J. Zhao, C. Xu, S.-G. Zhou, S. Wang, D. P. Sun, L. Liu, Z. Q. Li, N. B. Zhang, H. Jia, X. Q. Li, H. Hua, Q. B. Chen *et al.*, Phys. Rev. Lett. **116**, 112501 (2016).

[10] S. Bhattacharya, T. Trivedi, D. Negi, R. P. Singh, S. Muralithar, R. Palit, I. Ragnarsson, S. Nag, S. Rajbanshi, M. K. Raju, V. V. Parkar, G. Mohanto, S. Kumar, D. Choudhury, R. Kumar, R. K. Bhowmik, S. C. Pancholi, and A. K. Jain, Phys. Rev. C **100**, 014315 (2019).

[11] W. C. Haxton and E. M. Henley, Phys. Rev. Lett. **51**, 1937 (1983).

[12] J. Engel, M. J. Ramsey-Musolf, and U. van Kolck, Prog. Part. Nucl. Phys. **71**, 21 (2013).

[13] J. Dobaczewski, J. Engel, M. Kortelainen, and P. Becker, Phys. Rev. Lett. **121**, 232501 (2018).

[14] T. E. Chupp, P. Fierlinger, M. J. Ramsey-Musolf, and J. T. Singh, Rev. Mod. Phys. **91**, 015001 (2019).

[15] N. Auerbach, V. V. Flambaum, and V. Spevak, Phys. Rev. Lett. **76**, 4316 (1996).

[16] G. Maquart, L. Augey, L. Chaix, I. Companis, C. Ducoin, J. Dudouet, D. Guinet, G. Lehaut, C. Mancuso, N. Redon, O. Stézowski, A. Vancraeyenest, A. Astier, F. Azaiez, S. Courtin, D. Curien, I. Deloncle, O. Dorvaux, G. Duchêne, B. Gall *et al.*, Phys. Rev. C **95**, 034304 (2017).

[17] B. Ding, Z. Liu, D. Seweryniak, P. J. Woods, H. L. Wang, J. Yang, H. L. Liu, C. N. Davids, M. P. Carpenter, T. Davinson, R. V. F. Janssens, R. D. Page, A. P. Robinson, J. Shergur, S. Sinha, S. Zhu, X. D. Tang, J. G. Wang, T. H. Huang, W. Q. Zhang *et al.*, Phys. Rev. C **95**, 024301 (2017).

[18] R. Lică, G. Benzoni, A. I. Morales, M. J. G. Borge, L. M. Fraile, H. Mach, M. Madurga, C. Sotty, V. Vedia, H. D. Witte, J. Benito, T. Berry, N. Blasi, A. Bracco, F. Camera, S. Ceruti, V. Charviakova, N. Cieplicka-Oryńczak, C. Costache, F. C. L. Crespi *et al.*, J. Phys. G **44**, 054002 (2017).

[19] J. Wiśniewski, W. Urban, T. Rząca-Urban, A. G. Smith, J. F. Smith, G. S. Simpson, I. Ahmad, and J. P. Greene, Phys. Rev. C **96**, 064301 (2017).

[20] E. H. Wang, W. Lewis, C. J. Zachary, J. H. Hamilton, A. V. Ramayya, J. K. Hwang, S. H. Liu, N. T. Brewer, Y. X. Luo, J. O. Rasmussen, S. J. Zhu, G. M. Ter-Akopian, and Y. T. Oganessian, Eur. Phys. J. A **53**, 234 (2017).

[21] X. C. Chen, J. Zhao, C. Xu, H. Hua, T. M. Shneidman, S. G. Zhou, X. G. Wu, X. Q. Li, S. Q. Zhang, Z. H. Li, W. Y. Liang, J. Meng, F. R. Xu, B. Qi, Y. L. Ye, D. X. Jiang, Y. Y. Cheng, C. He, J. J. Sun, R. Han *et al.*, Phys. Rev. C **94**, 021301 (2016).

[22] E. Ruchowska, H. Mach, M. Kowal, J. Skalski, W. A. Płóciennik, and B. Fogelberg, Phys. Rev. C **92**, 034328 (2015).

[23] I. Ahmad, R. R. Chasman, J. P. Greene, F. G. Kondev, and S. Zhu, Phys. Rev. C **92**, 024313 (2015).

[24] W. Reviol, R. V. F. Janssens, S. Frauendorf, D. G. Sarantites, M. P. Carpenter, X. Chen, C. J. Chiara, D. J. Hartley, K. Hauschild, T. Lauritsen, A. Lopez-Martens, M. Montero, O. L. Pechenaya, D. Seweryniak, J. B. Snyder, and S. Zhu, Phys. Rev. C **90**, 044318 (2014).

[25] H. J. Li, S. J. Zhu, J. H. Hamilton, E. H. Wang, A. V. Ramayya, Y. J. Chen, J. K. Hwang, J. Ranger, S. H. Liu, Z. G. Xiao, Y. Huang, Z. Zhang, Y. X. Luo, J. O. Rasmussen, I. Y. Lee, G. M. Ter-Akopian, Y. T. Oganessian, and W. C. Ma, Phys. Rev. C **90**, 047303 (2014).

[26] T. Rząca-Urban, W. Urban, A. G. Smith, I. Ahmad, and A. Syntfeld-Każuch, Phys. Rev. C **87**, 031305 (2013).

[27] S. K. Tandel, M. Hemalatha, A. Y. Deo, S. B. Patel, R. Palit, T. Trivedi, J. Sethi, S. Saha, D. C. Biswas, and S. Mukhopadhyay, Phys. Rev. C **87**, 034319 (2013).

[28] T. Rząca-Urban, W. Urban, J. A. Pinston, G. S. Simpson, A. G. Smith, and I. Ahmad, Phys. Rev. C **86**, 044324 (2012).

[29] W. Reviol, D. G. Sarantites, C. J. Chiara, M. Montero, R. V. F. Janssens, M. P. Carpenter, T. L. Khoo, T. Lauritsen, C. J. Lister, D. Seweryniak, S. Zhu, O. L. Pechenaya, and S. G. Frauendorf, Phys. Rev. C **80**, 011304 (2009).

[30] N. J. Hammond, G. D. Jones, P. A. Butler, R. D. Humphreys, P. T. Greenlees, P. M. Jones, R. Julin, S. Juutinen, A. Keenan, H. Kettunen, P. Kuusiniemi, M. Leino, M. Muikku, P. Nieminen, P. Rahkila, J. Uusitalo, and S. V. Khlebnikov, Phys. Rev. C **65**, 064315 (2002).

[31] J. R. Hughes, R. Tölle, J. De Boer, P. A. Butler, C. Günther, V. Grafen, N. Gollwitzer, V. E. Holliday, G. D. Jones, C. Lauterbach, M. Marten-Tölle, S. M. Mullins, R. J. Poynter, R. S. Simon, N. Singh, R. J. Tanner, R. Wadsworth, D. L. Watson, and C. A. White, Nucl. Phys. A **512**, 275 (1990).

[32] R. Sheline, D. Decman, K. Nybo, T. Thorsteinsen, G. Lovhoiden, E. Flynn, J. Cizewski, D. Burke, G. Sletten, P. Hill, N. Kaffrell, W. Kurcewicz, G. Nyman, and G. Leander, Phys. Lett. B **133**, 13 (1983).

[33] G. A. Leander and R. K. Sheline, Nucl. Phys. A **413**, 375 (1984).

[34] G. A. Leander, W. Nazarewicz, P. Olanders, I. Ragnarsson, and J. Dudek, Phys. Lett. B **152**, 284 (1985).
[35] G. A. Leander and Y. S. Chen, Phys. Rev. C **37**, 2744 (1988).
[36] W. Sun, S. Quan, Z. P. Li, J. Zhao, T. Nikšić, and D. Vretenar, Phys. Rev. C **100**, 044319 (2019).
[37] N. Minkov, S. Drenska, P. Yotov, S. Lalkovski, D. Bonatsos, and W. Scheid, Phys. Rev. C **76**, 034324 (2007).
[38] N. Minkov and A. Pálffy, Phys. Rev. Lett. **118**, 212501 (2017).
[39] G. G. Adamian, N. V. Antonenko, R. V. Jolos, and T. M. Shneidman, Phys. Rev. C **70**, 064318 (2004).
[40] Y.-J. Chen, Z.-C. Gao, Y.-S. Chen, and Y. Tu, Phys. Rev. C **91**, 014317 (2015).
[41] Y. J. Chen, Y. S. Chen, Z. C. Gao, and Y. Tu, Int. J. Mod. Phys. E **24**, 1550081 (2015).
[42] Y. Huang, S. J. Zhu, J. H. Hamilton, Y. J. Chen, E. H. Wang, A. V. Ramayya, Z. G. Xiao, H. J. Li, Y. X. Luo, J. O. Rasmussen, G. M. Ter-Akopian, and Y. T. Oganessian, J. Phys. G **44**, 095101 (2017).
[43] C. Alonso, J. M. Arias, A. Frank, H. M. Sofia, S. M. Lenzi, and A. Vitturi, Nucl. Phys. A **586**, 100 (1995).
[44] M. Dahlinger, E. Kankeleit, D. Habs, D. Schwalm, B. Schwartz, R. Simon, J. Burrows, and P. Butler, Nucl. Phys. A **484**, 337 (1988).
[45] N. Amzal, P. A. Butler, G. D. Jones, D. Hawcroft, R. D. Herzberg, D. P. Rea, F. Hannachi, C. F. Liang, P. Paris, B. Gall, F. Hoellinger, and N. Schulz, Acta Phys. Pol. B **30**, 681 (1999).
[46] Y. Y. Wang, S. Q. Zhang, P. W. Zhao, and J. Meng, Phys. Lett. B **792**, 454 (2019).
[47] Y. P. Wang, Y. Y. Wang, and J. Meng, Phys. Rev. C **102**, 024313 (2020).
[48] Y. Y. Wang and S. Q. Zhang, Phys. Rev. C **102**, 034303 (2020).
[49] Y. Y. Wang, X. H. Wu, S. Q. Zhang, P. W. Zhao, and J. Meng, Sci. Bull. **65**, 2001 (2020).
[50] C. Morse, A. O. Macchiavelli, H. L. Crawford, S. Zhu, C. Y. Wu, Y. Y. Wang, J. Meng, B. B. Back, B. Bucher, C. M. Campbell, M. P. Carpenter, J. Chen, R. M. Clark, M. Cromaz, P. Fallon, J. Henderson, R. V. F. Janssens, M. D. Jones, T. L. Khoo, F. G. Kondev *et al.*, Phys. Rev. C **102**, 054328 (2020).
[51] I. Hamamoto, Nucl. Phys. A **271**, 15 (1976).
[52] I. Hamamoto and B. Mottelson, Phys. Lett. B **127**, 281 (1983).
[53] S. Q. Zhang, B. Qi, S. Y. Wang, and J. Meng, Phys. Rev. C **75**, 044307 (2007).
[54] S. G. Nilsson, Dan. Mat. Fys. Medd. **29**, 16 (1955).
[55] S. G. Nilsson, C. F. Tsang, A. Sobiczewski, Z. Szymański, S. Wycech, C. Gustafson, I.-L. Lamm, P. Möller, and B. Nilsson, Nucl. Phys. A **131**, 1 (1969).
[56] Y. Y. Wang and Z. X. Ren, Sci. China: Phys., Mech. Astron. **61**, 082012 (2018).
[57] F. S. Stephens, P. Kleinheinz, R. K. Sheline, and R. S. Simon, Nucl. Phys. A **222**, 235 (1974).
[58] P. Schüler, Ch. Lauterbach, Y. K. Agarwal, J. De Boer, K. P. Blume, P. A. Butler, K. Euler, Ch. Fleischmann, C. Günther, E. Hauber, H. J. Maier, M. Marten-Töllea, C. Schandera, R. S. Simon, R. Tölle, and P. Zeyen, Phys. Lett. B **174**, 241 (1986).
[59] P. Bonche, P. H. Heenen, H. Flocard, and D. Vautherin, Phys. Lett. B **175**, 387 (1986).
[60] S. Frauendorf, Phys. Rev. C **77**, 021304 (2008).
[61] R. V. Jolos, N. Minkov, and W. Scheid, Phys. Rev. C **72**, 064312 (2005).